



**Freestanding 1T MoS₂/Graphene Heterostructure as a
Highly Efficient Electrocatalyst for Lithium Polysulfides in
Li-S Batteries**

Journal:	<i>Energy & Environmental Science</i>
Manuscript ID	EE-ART-11-2018-003252
Article Type:	Paper
Date Submitted by the Author:	06-Nov-2018
Complete List of Authors:	He, Jiarui; University of Texas at Austin, Materials Science and Engineering Hartmann, Gregory; University of Texas at Austin Lee, Myungsuk; University of Texas at Austin, Chemical Engineering Hwang, Gyeong S.; University of Texas at Austin, Chemical Engineering Chen, Yuanfu; State Key Laboratory of Electronic Thin Films and Integrated Devices, University of Electronic Science and Technology of China Manthiram, Arumugam; University of Texas at Austin, Materials Science and Engineering



Journal Name

ARTICLE

Freestanding 1T MoS₂/Graphene Heterostructure as a Highly Efficient Electrocatalyst for Lithium Polysulfides in Li-S Batteries

Jiarui He^{a,b}, Gregory Hartmann^c, Myungsuk Lee^c, Gyeong S. Hwang^c, Yuanfu Chen,^{b*} and Arumugam Manthiram^{a*}

Received 00th January 20xx,
Accepted 00th January 20xx

DOI: 10.1039/x0xx00000x

www.rsc.org/

A novel approach to effectively suppress the “polysulfide shuttle” in Li-S batteries is presented by designing a freestanding, three-dimensional graphene/1T MoS₂ (3DG/TM) heterostructure with highly efficient electrocatalysis for lithium polysulfides (LiPSs). The 3DG/TM heterostructure is constructed by a few-layered graphene nanosheets sandwiched by hydrophilic, metallic, few-layered 1T MoS₂ nanosheets with abundant active sites. The porous 3D structure and the hydrophilic feature of 1T-MoS₂ are beneficial for electrolyte penetration and Li-ion transfer, and the high conductivities of both graphene and 1T MoS₂ nanosheets facilitate electron transfer. These merits lead to a high electrocatalytic efficiency for LiPSs due to excellent ion/electron transfer and sufficient electrocatalytic active sites. Therefore, the cells with 3DG/TM exhibit outstanding electrochemical performance, with a high reversible discharge capacity of 1181 mAh g⁻¹ and a capacity retention of 96.3% after 200 cycles. The electrocatalysis mechanism of LiPSs is further experimentally and theoretically revealed, which provides new insights and opportunities to develop advanced Li-S batteries with highly efficient electrocatalyst for LiPSs conversion.

Broader context

Advanced energy-storage technologies are urgently needed to satisfy the energy demands of society. Lithium-sulfur (Li-S) batteries are one of the most attractive candidates for next-generation energy-storage technology. However, it is extremely crucial to suppress the inherent polysulfide shuttle. Although electrocatalysis has been shown to enhance cell stability, further performance improvement of Li-S cells is seriously hindered due to a lack of understanding of the electrocatalysis mechanism on the sulfur redox process. Herein, for the first time, we design and synthesize a novel freestanding, three-dimensional graphene/1T MoS₂ (3DG/TM) heterostructure to improve the electrochemical performance and reveal the electrocatalysis mechanism. The well-designed 3DG/TM heterostructure can be used as a highly efficient electrocatalyst for the conversion of lithium polysulfides (LiPSs): the unique 3DG/TM nanoarchitecture, constructed by few-layered 2D MoS₂ nanosheets *in-situ* grown on porous 3D graphene network, guarantees abundant active sites, thus ensuring sufficient catalytic activity for LiPSs; the high conductivities of both the 3D graphene skeleton and the metallic 1T MoS₂ nanosheets (with conductivity six orders higher than that of 2H MoS₂) greatly accelerate the electron transfer; the rich porosity of 3DG/TM, along with the hydrophilic property of both 1T MoS₂ and 3DG, facilitates the electrolyte penetration and Li-ion transfer. Benefitting from these merits and synergistic effects, the cells with 3DG/TM exhibit large reversible specific capacity (1181 mAh g⁻¹) and outstanding long-term cycling stability. Furthermore, by combining post-mortem SEM and XPS characterizations and first-principles calculations, the electrocatalysis mechanism of LiPSs is clearly revealed, and the enhanced catalytic activity of the MoS₂-supported systems is mainly attributed to the enhanced binding and availability of LiPSs at the electrode interface. This work provides new insights and opportunities to develop advanced Li-S batteries with highly efficient electrocatalysts for LiPSs conversion.

Introduction

The spread of portable electronics and electric vehicles is prompting the development of energy storage systems with high-energy density and long-cycle life.¹⁻⁴ Of the many

alternatives, rechargeable lithium-sulfur (Li-S) batteries are one of the most attractive candidates as the next-generation energy storage technology, owing to their advantages, such as high theoretical energy density, nontoxicity, and low cost.⁵⁻⁸ However, the practical application of Li-S batteries is still hindered by several technical problems. For example, the insulating nature of sulfur and sulfides,⁹⁻¹³ limit electron transport in the cathode and lead to low active material utilization; in addition, the dissolution and migration of intermediate lithium polysulfides (LiPSs) result in a loss of the active material and shuttling of LiPSs.¹⁴⁻¹⁸

Recently, intensive research efforts, such as the fabrication of nanostructured carbon/sulfur composites, have led to an improvement in conductivity and cycling performance.¹⁹⁻²² However, since carbon materials provide poor adsorption

^a Materials Science and Engineering Program & Texas Materials Institute, The University of Texas at Austin, Austin, TX 78712, USA.
E-mail: manth@austin.utexas.edu

^b State Key Laboratory of Electronic Thin Films and Integrated Devices, University of Electronic Science and Technology of China, Chengdu 610054, PR China
E-mail: yfchen@uestc.edu.cn

^c McKetta Department of Chemical Engineering, The University of Texas at Austin, Austin, TX 78712, USA

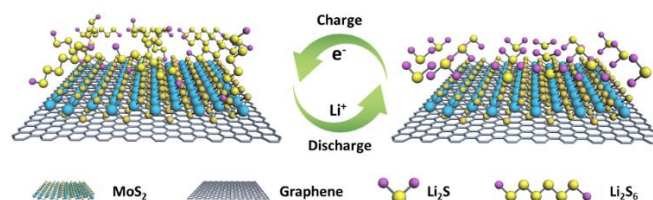
Electronic Supplementary Information (ESI) available: [details of any supplementary information available should be included here]. See DOI: 10.1039/x0xx00000x

toward LiPSs, limited loading of sulfur active material has been realized, which cannot meet the requirement for practical application of Li-S batteries.²³⁻²⁶ In order to improve the adsorption of LiPSs, polar hosts, such as metal compounds and metal-organic frameworks, have been developed.²⁷⁻³² On the one hand, polar hosts possess poor conductivity, which is detrimental to the kinetics of sulfur electrochemistry during cell operation, thus compromising the rate capability. On the other hand, most reports based on those hosts lack to deeply explore the mechanism of the electrochemical-performance enhancement. More recently, the electrocatalytic effect is recognized in metal- (*e.g.*, Pt, Au) and metal sulfide- (*e.g.*, CoS₂, WS₂) based sulfur hosts, which play a vital role in improving the reaction kinetics and suppressing the LiPSs shuttle process.³³⁻³⁶ However, as the catalysis of polysulfide conversion is still in a very early phase of research, the deep impact of the catalytic activity of the catalyst is still unclear, and thus the electrochemical performance based on the above mentioned cathodes is still far from realizing the full potential in Li-S batteries.

In this report, we present the synthesis of well-designed, freestanding, three-dimensional graphene/1T MoS₂ (3DG/TM) heterostructures as a highly efficient electrocatalyst for LiPSs conversion. The metallic 1T MoS₂ nanosheets are hydrophilic (Fig. S1a and b, ESI[†]) with rich active sites and high electronic conductivity that is six orders of magnitude higher than that of 2H MoS₂. The high electronic conductivity facilitates fast electron transfer, the hydrophilic property benefits ion diffusion, and the dense active sites ensure sufficient catalytic activity for LiPSs. The 3DG/TM heterostructures of our designed material can maximize the aspect ratio of active catalytic sites. The freestanding, porous morphology of the 3DG/TM material facilitates electrolyte accessibility (Fig. S1c and d, ESI[†]), enabling better ion transport. Benefitting from these synergistic effects (**Scheme**), the cells with 3DG/TM exhibit excellent specific capacity and outstanding cycling stability. Furthermore, the fundamental understanding for the enhanced catalytic activity in the MoS₂-supported systems is revealed via experimental characterizations and theoretical calculation, which provide new insights and opportunities to develop advanced Li-S batteries with highly efficient electrocatalysts for LiPSs. Based on the deep understanding of the electrocatalysis of LiPSs conversion, the well-designed 3DG/TM heterostructures with rich electrocatalytically active sites ensure high catalytic activity and thus significantly improve the electrochemical performance of Li-S batteries. Even with a very high sulfur loading (10 mg cm⁻²), the S/3DG/TM cathode not only effectively mitigates the LiPS shuttling, but also delivers excellent specific capacity, outstanding rate capability, and pronounced cycling stability for an impressive number of 500 cycles.

It is believed that the structure of the electrocatalyst plays a vital role in catalytic activity. Therefore, we present a well-designed electrocatalyst of three-dimensional graphene/1T MoS₂ (3DG/TM) heterostructures synthesized through a facile one-pot hydrothermal process. The graphene/MoS₂ hydrogel of was formed by a hydrothermal reaction using MoO₃, thioacetamide, and graphene oxide as starting materials; during

the hydrothermal reaction, 1T MoS₂ was *in-situ* formed on the surface of graphene oxide owing to its abundant functional groups and defects.³⁷⁻³⁹ Then, a self-assembled 3DG/TM aerogel with graphene/1T MoS₂ heterostructures was obtained by simply freeze drying the hydrogel to remove water, as further described in the supplementary information.



Scheme. The conversion process of LiPSs on a graphene surface with 1T MoS₂. The 3DG/TM heterostructures work as a highly efficient electrocatalyst for LiPSs conversion.

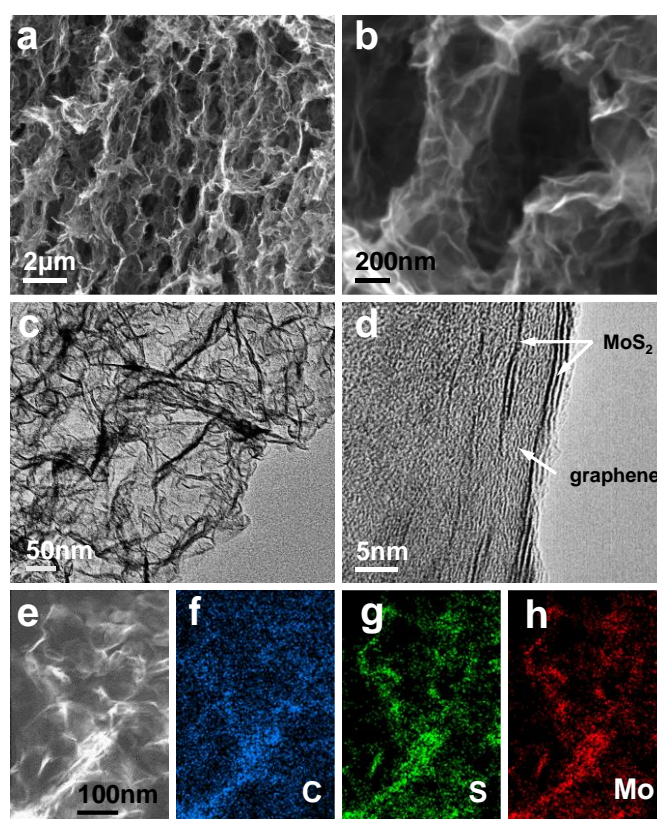


Fig. 1 Morphological characterizations of 1T MoS₂ on graphene aerogel. (a, b) SEM of the porous 3DG/TM. (c) Low-magnification TEM images of 3DG/TM. (d) High-magnification TEM images of 3DG/TM. (e) TEM morphologies of 3DG/TM, and the corresponding elemental mapping images of (f) carbon, (g) sulfur, and (h) molybdenum.

As shown in Fig. S2 (ESI[†]), the 3DG/TM aerogel is a freestanding electrode with high flexibility that can be cut and compressed easily. In order to reveal the structure of the 3DG/TM, scanning electron microscopy (SEM) was performed. The morphology of the 3DG/TM is shown in **Fig. 1**. Fig. 1a and 1b indicate that the 3DG/TM are composed of graphene/1T MoS₂ nanosheets, which cross-link to form a 3D interconnected

network with rich pores. The SEM images in Fig. S3 (ESI[†]) show that 3DG/HM and 3DG also have a porous architecture. Such a porous structure can not only facilitate electrolyte accessibility, which benefits ion transport, but also provide a large number of active sites for the reaction. The TEM image in Fig. 1c further confirms that the graphene/1T MoS₂ nanosheets in 3DG/TM are very thin. The high-resolution TEM image in Fig. 1d shows the graphene/1T MoS₂ heterostructures in 3DG/TM.⁴⁰ Such a unique structure can provide a high aspect ratio of edge sites and accessibility of a large catalytic surface, which is beneficial for the electrocatalytic reaction. The elemental mappings of C, S, and Mo in Fig. 1f – g illustrate the uniform distribution of MoS₂ on the graphene surface.

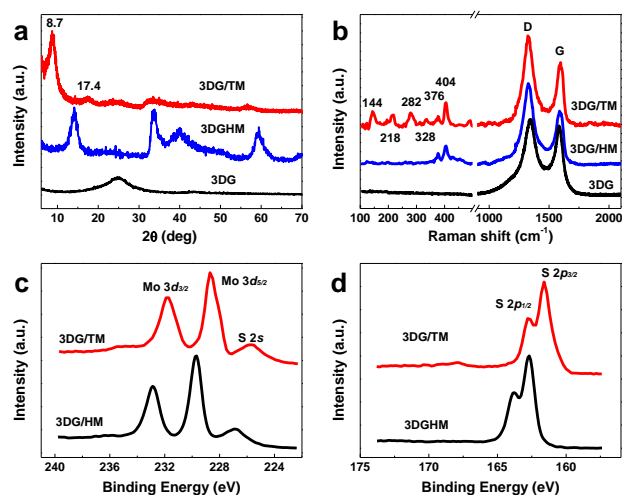


Fig. 2 (a) XRD patterns and (b) Raman shift of 3DG/TM, 3DG/HM, and 3DG. High-resolution XPS spectra of Mo 3d (c) and S 2p (d) for 3DG/TM and 3DG/HM.

In order to identify the influence of structure on catalytic activity, three dimensional graphene/2H MoS₂ (3DG/HM) and three-dimensional graphene (3DG) were prepared as well. Fig. 2a shows the X-ray diffraction (XRD) pattern of 3DG/TM in comparison with 3DG/HM and 3DG. As the XRD patterns show in Fig. 2a, in contrast to the (002) peak at 14.18° in 3DG/HM, the XRD pattern of 3DG/TM shows two peaks at 8.7° and 17.4° corresponding to the (002) and (004) planes of 1T MoS₂, which matches well with the previous report on 1T MoS₂.⁴¹ Interestingly, the (002) peak of 3DG cannot be detected in the pattern of 3DG/TM, indicating that the graphene nanosheets do not stack during the hydrothermal synthesis process. Fig. 2b shows the Raman spectra of 3DG/TM, 3DG/HM, and 3DG. A strong Raman band is observed at 144 cm⁻¹, which corresponds to the Mo-Mo stretching vibrations in 1T MoS₂ in 3DG/TM. The intense peaks at 218, 282, and 328 cm⁻¹ are attributed to the phonon modes of 1T MoS₂.⁴² 3DG/HM exhibits typical Raman shifts of 376 and 405 cm⁻¹ corresponding to the E_{2g} and A_{1g} modes, respectively, which are substantially different from those of 3DG/TM.⁴² All samples show peaks at 1325 and 1596 cm⁻¹ corresponding to the D band and G band of graphene.⁴³

The phase identification of the prepared 3DG/TM and 3DG/HM was further investigated by X-ray photoelectron

spectroscopy (XPS). Fig. 2c shows the high-resolution XPS spectra of Mo 3d, in which the peaks observed at 228.7 and 231.8 eV correspond to the 3d_{5/2} and 3d_{3/2} components of Mo⁴⁺ of 1 T MoS₂ in 3DG/TM. The peaks of Mo 3d in 3DG/HM are shifted to higher binding energies by 1 eV compared to those of 3DG/TM. Such results match well with previous reports.⁴² Similarly, as shown in Fig. 2d, the S 2p spectra of 3DG/TM consist of peaks at 161.8 and 162.9 eV, associated with S 2p_{3/2} and 2p_{1/2}, which are lower than the corresponding peaks in 3DG/HM. These spectra indicate pure 1T MoS₂ in 3DG/TM. Thermogravimetric analysis (TGA), shown in Fig. S4 (ESI[†]), demonstrates the content of 1T MoS₂ in 3DG/TM is 25.2 wt.%. For a fair comparison, the 2H MoS₂ in 3DG/HM is controlled same as that of 3DG/TM Fig. S4 (ESI[†]).

In order to demonstrate the advantages of 3DG/TM as an electrocatalyst towards LiPSs conversion, electrochemical tests were performed with a three-electrode system. The electrocatalyst was coated onto glassy carbon (GC) as the working electrode, lithium foil was used as the counter electrode, Pt foil was used as reference electrode, and a 10 mM Li₂S₆ solution was used as electrolyte. The electrocatalyst (3DG/TM, 3DG/HM, or 3DG) was loaded onto GC with 5 wt.% Nafion solution as reported previously in the literature.¹ Fig. 3a - c shows the representative cyclic voltammetry (CV) curves and lithium-ion diffusion characteristics based on the three-electrode system. Corresponding parameters, such as the open-circuit voltage (OCV), anodic peak potential (E_{pa}), cathodic peak potential (E_{pc}), anodic peak current density (I_{pa}), cathodic peak current density (I_{pc}), and lithium-ion diffusivity (D_{Li+}) are given in Table S1 (ESI[†]). The E_{pa} related to oxidation of LiPSs with 3DG/TM electrode is 2.40 V, a negative shift compared to 2.43 V for the 3DG/HM and 2.51 V for 3DG, under identical experimental conditions. Similarly, for 3DG/TM, the observed E_{pc} corresponding to the reduction of LiPSs is 2.29 V, with a positive shift compared to that of 3DG/HM (2.28 V). Importantly, the E_{pc} of 3DG is missing, which can be explained as follows: during the oxidation process, the LiPSs converts to S₈ on the surface of the electrocatalyst. Therefore, only if the electrocatalysts have strong affinity to LiPSs/Li₂S/S₈, the reversible transformation can be realized. In addition, all the electrocatalysts (3DG, 3DG/HM, and 3DG/TM) have close specific surface area and pore size distribution (Fig. S5, ESI[†]). Therefore, differences in the electrocatalytic performance mainly come from the catalytic activity of the materials. Owing to the poor interaction between 3DG and S₈/LiPSs, the oxidation product of LiPSs (S₈) desorb from the surface of 3DG. Thus, the reduction peak of 3DG cannot be detected. The LiPSs adsorption tests shown in Fig. S6 (ESI[†]) confirm the strong interaction of 3DG/TM towards LiPSs. Furthermore, the CV curves of the three-electrode system with 3DG/TM remain stable, as shown in Fig. S7 (ESI[†]), suggesting outstanding durability of 3DG/TM.

In addition, 3DG/TM shows the highest current densities (I_{pa} and I_{pc}), suggesting that the 3DG/TM has superior catalytic ability, as shown in Table S1. To obtain the kinetic behavior of each electrocatalyst, linear sweep voltammograms (LSV) at different scan rates were employed (Fig. 3b, Fig. S8, and Fig. S9,

ESI[†]). The peak current densities for the 3DG/TM electrode in comparison with 3DG/HM and 3DG electrode vs. the square root of the scan rates are shown in Fig. 3c. The lithium-ion diffusivity can be determined utilizing the classical Randles-Sevcik equation: $i_p = (2.69 \times 10^5) n^{1.5} S D_{Li^+}^{0.5} C_{Li} v^{0.5}$, where i_p is the peak current, n is the charge-transfer number, S

is the geometric area of the active electrode, D_{Li^+} is the lithium-ion diffusion coefficient, C_{Li} is the concentration of lithium ions in the cathode, and v is the potential scan rate.⁴⁴ According to the calculated D_{Li^+} , it can be clearly seen that the 3DG/TM exhibits the highest lithium-ion diffusivity, which is further evidence of the high catalytic activity of 3DG/TM.

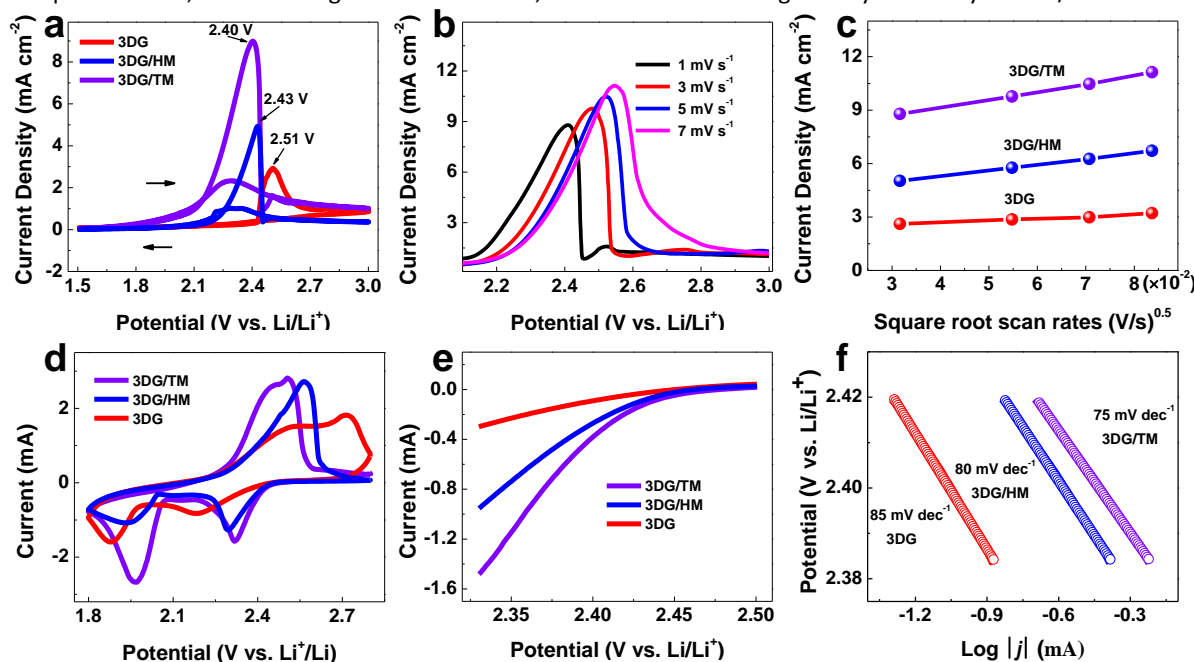


Fig. 3 (a) Comparative CV of 3DG/TM and 3DG electrodes vs. Li/Li⁺ in a catholyte solution. (b) LSV of 3DG/TM electrode with 10 mM Li₂S₆ based electrolyte at various scan rates. (c) peak current for the 3DG/TM electrode in-comparison with 3DG/HM and 3DG electrode vs. the square root of the scan rates and (d) CV of Li-S batteries with Li as the anode and 3DG/TM, 3DG/HM and 3DG with catholyte consisting of 1 M Li₂S₆ as the cathode at a scan rate of 0.1 mV s⁻¹ between 1.8 and 2.8 V. (e) potentiostatic polarization curve of 3DG/TM, 3DG/HM, and 3DG electrodes at a scan rate of 0.1 mV s⁻¹ for charging and discharging process. (f) Tafel plots derived from the potentiostatic polarization curves.

The binding strength of LiPSs on free-standing and MoS₂-supported graphene was evaluated by dispersion-corrected DFT (DFT-D3) calculations. Details of the computational methods and model structures (Fig. S10 – S12, ESI[†]) employed are described in the ESI[†]. We assume the following route for the redox reaction between S₈ and Li₂S during the charge cycle: $8Li_2S \rightleftharpoons 16Li^+ + 16e^- + S_8$. The binding energy (E_b) is obtained by subtracting the total energy of the LiPS/slab system ($E_{LiPS/slab}$) from the sum of the slab (E_{slab}) and LiPS species (E_{LiPS}) energies (i.e., $E_b = E_{slab} + E_{LiPS} - E_{LiPS/slab}$). As shown in Fig. 4, the results clearly demonstrate LiPSs to be more strongly bound to graphene supported on MoS₂ than on free-standing graphene, while the increase in E_b tends consistently to be larger in the case of G/1T compared to G/2H. The E_b of Li₂S and S₈ in G/1T compared to G are enhanced by 0.13 eV and 0.16 eV, respectively. Other intermediate species also show an increase in E_b by a similar order of magnitude. The E_b difference between the G/1T and G/2H systems tends to become distinct for lower molecular weight LiPSs (Li₂S_n, n ≤ 4); for Li₂S, the E_b is enhanced by 0.08 eV in G/1T compared to G/2H. In each case, the binding of LiPSs to bare MoS₂ is significantly stronger compared to that for the graphene basal planes, and the binding energy of each system is in agreement with the previously reported values.^{45, 46}

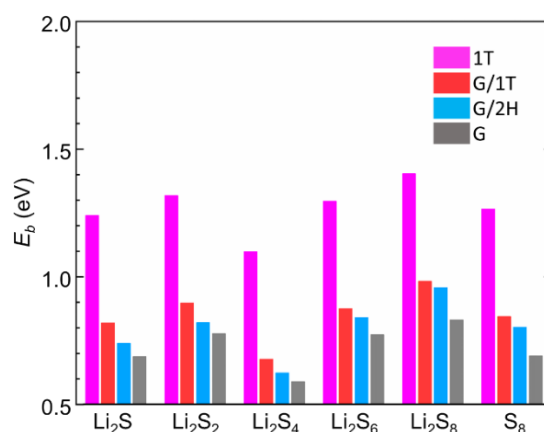


Fig. 4 Binding energies of LiPS on MoS₂, MoS₂-supported graphene, and pristine graphene.

Classical force field calculations were also performed to evaluate the adhesion of MoS₂ on corrugated graphene (see ESI[†] for details). As illustrated in Fig. S13, MoS₂ exhibits high-fidelity conformation to graphene topographic features, although it may not conform well to the relatively small jagged features of the graphene surface. This may serve not only to possibly produce distorted and activated MoS₂ surfaces, but

possibly can increase the interlayer spacing of few-layer MoS₂, allowing LiPSs to diffuse between the layers and dramatically increasing the available surface area. Together, experiment and theory suggest that the enhanced catalytic activity in the MoS₂-supported systems is primarily due to the increased MoS₂ surface area and availability of LiPSs at the electrode interface.

To further confirm the advantages of 3DG/TM as an electrocatalyst for the conversion of LiPSs, standard 2032 coin cells were assembled with the freestanding 3DG/TM, 3DG/HM, and 3DG aerogels, catholyte consisting of 1 M Li₂S₆ as cathode, lithium foil as anode, and Celgard membrane as a separator. As shown in Fig. 3d, the CV curve of the cells with 3DG/TM consist of two cathodic peaks at 2.32 and 1.97 V, which can be attributed to the conversion of long-chain LiPSs to short-chain LiPSs and finally to Li₂S. In the subsequent anodic scan, the anodic peak at 2.50 V corresponds to the reversible transformation of Li₂S to LiPSs and ultimately to elemental sulfur. Such a reversible conversion further illustrates the excellent catalytic activity. It is noted that the 3DG/TM displays a distinguishable positive shift in the cathodic peak and negative shift in anodic peak along with much higher current density with respect to 3DG/HM and 3DG, in agreement with the phenomena observed in the three-electrode system and further confirming a significant improvement in the catalytic activity of 3DG/TM towards LiPSs conversion. Accordingly, the onset potential for the oxidation of long-chain LiPSs to short-chain LiPSs in 3DG/TM is reduced compared to 3DG/HM and 3DG (Fig. 3e). Tafel plots are obtained from Fig. 3e for the identification of the electrocatalytic effect on the charge-transfer kinetics during LiPSs conversion, as shown in Fig. 3f. The 3DG/TM displays a lower Tafel slope (76 mV dec⁻¹) compared to those of 3DG/HM (81 mV dec⁻¹) and (87 mV dec⁻¹). The significant

decrease in Tafel slope values of 3DG/TM confirms the accelerated rate of Li-S redox conversion.

The electrocatalysts of 3DG/TM and 3DG coated on the glassy carbon after scanning from 1.5 to 3 V were visualized via SEM. SEM images of 3DG/TM and 3DG before and after scanning are shown in Fig. 5a – d. The nanosheets in 3DG/TM become thick, attributed to the conversion and accumulation of sulfur at electrocatalytically active sites. In a sharp contrast, the morphologies of 3DG before and after scanning remain unchanged. The unchanged morphology indicates that few sulfur particles deposit on the surface of 3DG, resulting from the weak interactions with LiPSs/sulfur. The XPS results in Fig. 5e and 3f support this explanation. The high-resolution S 2p spectra of 3DG/TM at different states are shown in Fig. 5e. When the cell was scanned to 3.0 V, the peaks at 164.9 and 163.6 eV are attributed to the sulfur on the nanosheets of 3DG/TM. The new features between 168 and 172 eV are due to the thiosulfate and polythionate species formed by the redox reaction between LiPSs and the 1T MoS₂ in 3DG/TM, as is consistent with the previous reports.⁴² When the cell was scanned to the E_{pc}, the sulfur on the 3DG/TM can be efficiently reduced to LiPSs; therefore, the sulfur peaks diminish. On the other hand, limited sulfur deposited on the surface of 3DG when the cell was scanned to 3.0 V, as shown by the weak intensity of sulfur peaks observed in Fig. 5f. When the cell was returned to 2.29 V from 3.0 V, the weak peak detected at 165 - 161 eV can be attributed to the minor residual LiPSs in the 3DG. XPS analyses agree with the results in CV, and further reveal the excellent electrocatalytic effect of 3DG/TM towards LiPSs conversion.

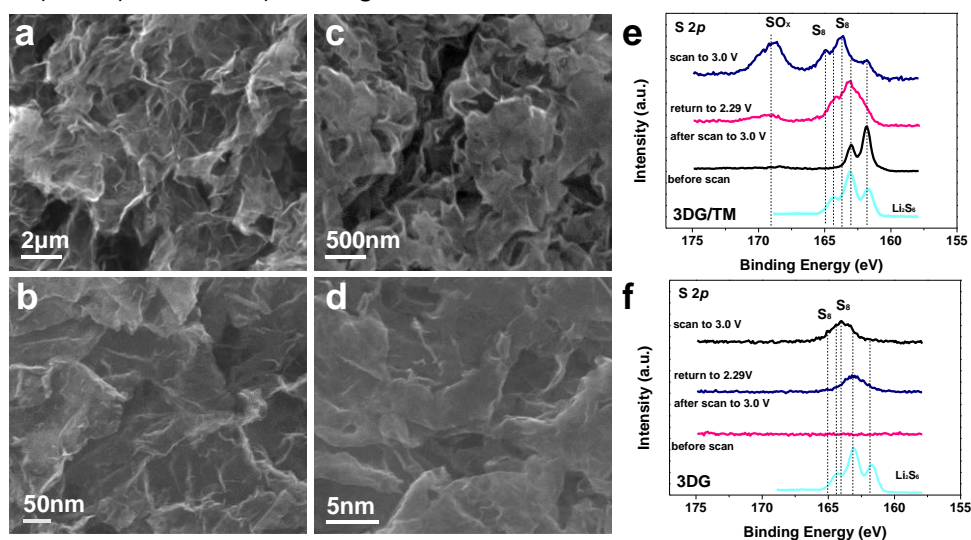


Fig. 5 SEM images of (a) the pristine 3DG/TM electrode and (b) the 3DG/TM working electrode removed from the three-electrode system after scanning to 2.4 V; (c) the pristine 3DG electrode and (d) the 3DG working electrode after scanning to 3.0 V. XPS spectra of the (e) 3DG/TM and (f) 3DG working electrodes of the three-electrode system after scanning to 3.0 V, or after scanning to 3.0 V and returning to 2.29 V

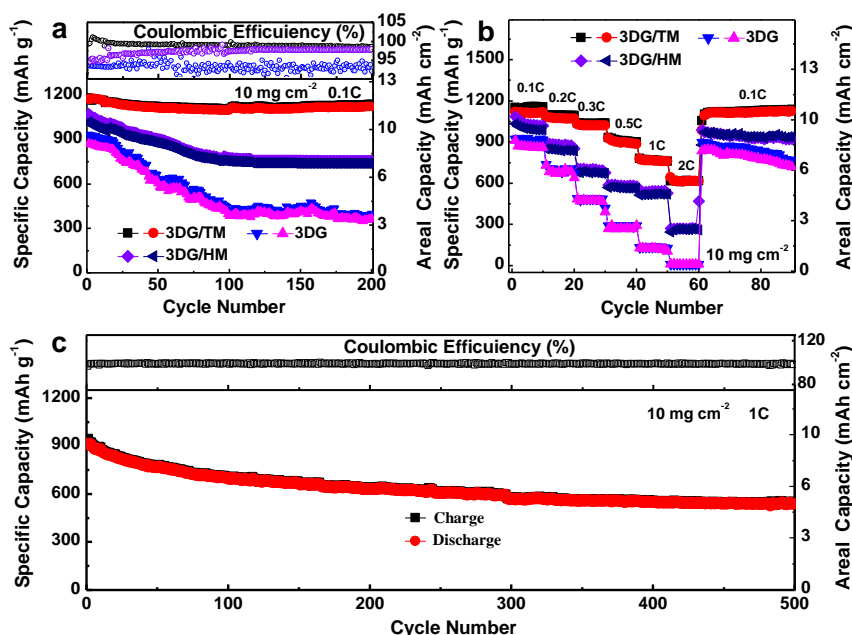


Fig. 6 (a) Cyclic stability of electrocatalytically active 3DG, 3DG/HM, and 3DG/TM as working electrode vs. Li/Li⁺ with a catholyte consisting of 1 M Li₂S₆ at 0.1C rate. (b) Rate performances at various cycling rates of the 3DG/TM with catholyte. (c) Long-term cycling cyclability of 3DG/TM with catholyte at 1C rate.

The long-term cyclability is a key factor to evaluate the catalytic stability, which is further examined in 2032 coin cells with metallic Li as the anode and the freestanding 3DG/TM, 3DG/HM, and 3DG with a catholyte consisting of 1 M Li₂S₆ as cathode. As shown in Fig. 6a, the cell with 3DG/TM exhibits superior performance, with a highly reversible discharge capacity of 1,181 mAh g⁻¹ and a capacity retention of 96.3% after 200 cycles. In contrast, the cells with 3DG/HM and 3DG display poor cyclic performance, with a low capacity retention of 72.6% and 42.6%, due to the limited catalytically active sites. It is noted that the coulombic efficiency of 3DG/TM is the highest compared to those of 3DG/HM and 3DG, which further confirms that the high electrocatalytic ability of 3DG/TM can significantly mitigate the LiPS shuttling. The photographs of the the separators and lithium foils extracted from cells with 3DG, 3DG/HM, and 3DG/TM after 200 cycles indicate that the LiPS dissolution is remarkably suppressed in Li-S cells with 3DG/TM (Fig. S14a - f, ESI[†]). The corrosion depths on those lithium foils were also obtained from the cross-sectional SEM morphologies of the cycled lithium foil paired with 3DG, 3DG/HM, and 3DG/TM (Fig. S14g - i, ESI[†]). The lithium foil paired with 3DG/TM shows the smallest corrosion depth, which clearly demonstrates the significant mitigation of LiPS shuttling.

The rate performance reflects redox reaction kinetics of the Li-S battery. The cells with 3DG/TM, 3DG/HM, and 3DG were also cycled under various C-rates. As shown in Fig. 6b and Fig. S15 - Fig. S17 (ESI[†]), the high capacity of 613 mAh g⁻¹ at the rate of 2C of the cell with 3DG/TM directly illustrates the accelerated rate of Li-S redox conversion in 3DG/TM. In contrast, the cells with 3DG/HM and 3DG exhibit inferior rate performance, owing to the slow kinetics towards LiPSs conversion. More importantly, compared to 3DG/HM and 3DG, the EIS spectrum

of 3DG/TM after 200 cycles (Fig. S18, ESI[†]) suggests that the cell with 3DG/TM has high redox kinetics, which matches well with the rate capability results. To further determine whether the 3DG/TM can retain the high redox kinetics during long-term cycling, the prolonged cycling performance of the cells with 3DG/TM was evaluated at 1C rate for 500 cycles (Fig. 6c). The cell with 3DG/TM exhibits outstanding cyclic performance at a high rate of 1C for 500 cycles with a low capacity fading of 0.08% per cycle. Such appreciable cyclic performance directly demonstrates that 3DG/TM can maintain fast redox kinetics and remain stable even under super long-term cycles. The excellent electrochemical performance of the cells with 3DG/TM complements the electrocatalytic analyses, which further confirms the outstanding electrocatalytic activity of 3DG/TM.

Conclusions

In summary, we have designed and synthesized freestanding, three-dimensional graphene/1T MoS₂ (3DG/TM) heterostructures as a highly efficient electrocatalyst for polysulfides. The metallic 1T MoS₂ nanosheets are hydrophilic with rich active sites. The high electronic conductivity of 1T MoS₂ facilitate electron transfer, while the dense active sites ensure sufficient catalytic activity for LiPSs. The 3DG/TM with heterostructures can maximize the aspect ratio of active catalytic sites, and the freestanding, hydrophilic feature of the 3DG/TM porous nanoarchitecture can facilitate electrolyte accessibility, thus enhancing ion transport. Benefiting from these synergistic effects, the cells with 3DG/TM exhibit excellent specific capacity and outstanding cycling stability. Moreover, experiment and theory suggest that the enhanced catalytic activity in the MoS₂-supported systems is primarily due

to the enhanced binding and availability of LiPSs at the electrode interface. The fundamental understanding on electrocatalysis of polysulfides can provide new insights and opportunities to develop advanced Li-S batteries.

Conflicts of interest

There are no conflicts to declare.

Acknowledgements

This work was primarily supported by the U.S. Department of Energy, Office of Basic Energy Sciences, Division of Materials Science and Engineering under award number DE-SC0005397. The TEM work was supported by National Natural Science Foundation of China (Grant No. 21773024). The computational work was supported by the Welch Foundation grant F-1535. The authors thank the Texas Advanced Computing Center (TACC) for providing HPC resources. The authors thank Prof. Yang Xia and Ms. Martha Gross for helpful discussion.

Notes and references

- 1 L. Li, S. Chai, S. Dai, A. Manthiram, *Energ. Environ. Sci.* 2014, **7**, 2630.
- 2 F. Wu, T. P. Pollard, E. Zhao, Y. Xiao, M. Olguin, O. Borodin, G. Yushin, *Energ. Environ. Sci.* 2018.
- 3 Y. You, X. Wu, Y. Yin, Y. Guo, *Energ. Environ. Sci.* 2014, **7**, 1643.
- 4 Y. Fu, A. Manthiram, *J. Phys. Chem. C* 2012, **116**, 8910.
- 5 J. Zhou, R. Li, X. Fan, Y. Chen, R. Han, W. Li, J. Zheng, B. Wang, X. Li, *Energ. Environ. Sci.* 2014, **7**, 2715.
- 6 Y. Yang, G. Zheng, Y. Cui, *Energ. Environ. Sci.* 2013, **6**, 1552.
- 7 G. Zhou, E. Paek, G. S. Hwang, A. Manthiram, *Nat. Commun.* 2015, **6**, 7760.
- 8 Y. Fu, Y. Su, A. Manthiram, *Adv. Energy Mater.* 2014, **4**, 201300655.
- 9 Z. Li, J. Zhang, Y. Lu, X. W. D. Lou, *Sci. Adv.* 2018, **4**, t1687.
- 10 M. J. Klein, G. M. Veith, A. Manthiram, *J. Am. Chem. Soc.* 2017, **139**, 9229.
- 11 M. J. Klein, G. M. Veith, A. Manthiram, *J. Am. Chem. Soc.* 2017, **139**, 10669.
- 12 Y. Fu, C. Zu, A. Manthiram, *J. Am. Chem. Soc.* 2013, **135**, 18044.
- 13 H. Xu, S. Wang, A. Manthiram, *Adv. Energy Mater.* 2018, 1800813.
- 14 C. Nan, Z. Lin, H. Liao, M. Song, Y. Li, E. J. Cairns, *J. Am. Chem. Soc.* 2014, **136**, 4659.
- 15 J. He, Y. Chen, W. Lv, K. Wen, C. Xu, W. Zhang, Y. Li, W. Qin, W. He, *ACS Nano* 2016, **10**, 10981.
- 16 J. He, Y. Chen, P. Li, F. Fu, Z. Wang, W. Zhang, *J. Mater. Chem. A* 2015, **3**, 18605.
- 17 T. Lei, W. Chen, J. Huang, C. Yan, H. Sun, C. Wang, W. Zhang, Y. Li, J. Xiong, *Adv. Energy Mater.* 2016, 1601843.
- 18 W. Chen, T. Qian, J. Xiong, N. Xu, X. Liu, J. Liu, J. Zhou, X. Shen, T. Yang, Y. Chen, C. Yan, *Adv. Mater.* 2017, **29**, 1605160.
- 19 R. Fang, S. Zhao, P. Hou, M. Cheng, S. Wang, H. Cheng, C. Liu, F. Li, *Adv. Mater.* 2016, **28**, 3374.
- 20 G. Zhou, S. Pei, L. Li, D. Wang, S. Wang, K. Huang, L. Yin, F. Li, H. Cheng, *Adv. Mater.* 2014, **26**, 625.
- 21 J. Zhang, C. Yang, Y. Yin, L. Wan, Y. Guo, *Adv. Mater.* 2016, **28**, 9539.
- 22 S. Xin, L. Gu, N. Zhao, Y. Yin, L. Zhou, Y. Guo, L. Wan, *J. Am. Chem. Soc.* 2012, **134**, 18510.
- 23 X. Liu, J. Huang, Q. Zhang, L. Mai, *Adv. Mater.* 2017, **29**, 1601759.
- 24 A. Manthiram, S. Chung, C. Zu, *Adv. Mater.* 2015, **27**, 1980.
- 25 C. Milroy, A. Manthiram, *Adv. Mater.* 2016, **28**, 9744.
- 26 J. He, Y. Chen, A. Manthiram, *Energ. Environ. Sci.* 2018, **11**, 2560.
- 27 J. He, L. Luo, Y. Chen, A. Manthiram, *Adv. Mater.* 2017, **29**, 1702707.
- 28 Z. Xiao, Z. Yang, L. Wang, H. Nie, M. Zhong, Q. Lai, X. Xu, L. Zhang, S. Huang, *Adv. Mater.* 2015, **27**, 2891.
- 29 Z. Cui, C. Zu, W. Zhou, A. Manthiram, J. B. Goodenough, *Adv. Mater.* 2016, **28**, 6926.
- 30 Y. Zhang, Z. Mu, C. Yang, Z. Xu, S. Zhang, X. Zhang, Y. Li, J. Lai, Z. Sun, Y. Yang, Y. Chao, C. Li, X. Ge, W. Yang, S. Guo, *Adv. Funct. Mater.* 2018, **28**, 1707578.
- 31 M. Wang, L. Fan, D. Tian, X. Wu, Y. Qiu, C. Zhao, B. Guan, Y. Wang, N. Zhang, K. Sun, *ACS Energy Lett.* 2018, **3**, 1627.
- 32 Y. C. Jeong, J. H. Kim, S. H. Kwon, J. Y. Oh, J. Park, Y. Jung, S. G. Lee, S. J. Yang, C. R. Park, *J. Mater. Chem. A* 2017, **5**, 23909.
- 33 G. Babu, K. Ababtain, K. Y. S. Ng, L. M. R. Arava, *Sci. Rep.* 2015, **5**.
- 34 H. Al Salem, G. Babu, C. V. Rao, L. M. R. Arava, *J. Am. Chem. Soc.* 2015, **137**, 11542.
- 35 Z. Yuan, H. Peng, T. Hou, J. Huang, C. Chen, D. Wang, X. Cheng, F. Wei, Q. Zhang, *Nano Lett.* 2016, **16**, 519.
- 36 G. Babu, N. Masurkar, H. Al Salem, L. M. R. Arava, *J. Am. Chem. Soc.* 2016, **139**, 171.
- 37 K. Chang, D. Geng, X. Li, J. Yang, Y. Tang, M. Cai, R. Li, X. Sun, *Adv. Energy Mater.* 2013, **3**, 839.
- 38 Y. Li, H. Wang, L. Xie, Y. Liang, G. Hong, H. Dai, *J. Am. Chem. Soc.* 2011, **133**, 7296.
- 39 J. He, P. Li, W. Lv, K. Wen, Y. Chen, W. Zhang, Y. Li, W. Qin, W. He, *Electrochim. Acta* 2016, **215**, 12.
- 40 X. Geng, Y. Jiao, Y. Han, A. Mukhopadhyay, L. Yang, H. Zhu, *Adv. Funct. Mater.* 2017, 1702998.
- 41 Q. Liu, X. Li, Q. He, A. Khalil, D. Liu, T. Xiang, X. Wu, L. Song, *Small* 2015, **11**, 5556.
- 42 X. Geng, W. Sun, W. Wu, B. Chen, A. Al-Hilo, M. Benamara, H. Zhu, F. Watanabe, J. Cui, T. Chen, *Nat. Commun.* 2016, **7**, 10672.
- 43 J. He, Y. Chen, W. Lv, K. Wen, Z. Wang, W. Zhang, Y. Li, W. Qin, W. He, *ACS Nano* 2016, **10**, 8837.
- 44 G. Zhou, H. Tian, Y. Jin, X. Tao, B. Liu, R. Zhang, Z. W. Seh, D. Zhuo, Y. Liu, J. Sun, J. Zhao, C. Zu, D. S. Wu, Q. Zhang, Y. Cui, *Proc. Natl. Acad. Sci. USA* 2017, **114**, 840.
- 45 Y. C. Jeong, J. H. Kim, S. H. Kwon, J. Y. Oh, J. Park, Y. Jung, S. G. Lee, S. J. Yang, C. R. Park, *J. Mater. Chem. A* 2017, **5**, 23909.
- 46 S. P. Jand, Y. Chen, P. Kaghazchi, *J. Power Sources* 2016, **308**, 166.